JOURNAL OF THERMOPHYSICS AND HEAT TRANSFER
Vol. 14, No. 3, July–September 2000

Energy Partitions in Inductively Heated Plasma Sources for Reentry Simulations

S. Lenzner,* M. Auweter-Kurtz,† and J. Heiermann‡
University of Stuttgart, D-70550 Stuttgart, Germany
and
P. C. Sleziona§
Institut für Techno- und Wirtschaftsmathematik e.V., D-67663 Kaiserslautern, Germany

An inductively heated radio-frequency plasma source for reentry simulations has been developed at the Institute of Space Systems of the University of Stuttgart. This plasma source can be investigated by plasma diagnostic techniques, as well as by numerical methods. A numerical code has been developed to compute the plasma state properties in the discharge region of this plasma source for four-species ionized argon flow. The electric input power, the total jet enthalpy, and the heat flux to the confinement tube wall can be computed to investigate these energy partitions. Further improvements need to be made to the code to decrease the computation time to perform parameter studies for optimizing the thermal efficiency of this plasma source. A simplified code that computes the plasma properties of an entire subsonic flowfield under atmospheric pressure conditions was used to test these kind of parameter studies. Results are presented of the plasma flow quantities in this plasma source for an argon discharge under low-pressure conditions of a reentry simulation. Additionally, results of numerically performed parameter studies for an argon discharge under atmospheric pressure conditions are discussed.

Nomenclature

$\boldsymbol{A}$	= vector potential
$\boldsymbol{B}$	= magnetic induction
c	= velocity of light
c_i	= molar concentration
D	= diffusion coefficient
$\boldsymbol{E}$	= electric field strength
e	= elementary charge
e_*	= mass specific energy
$G(k)$	= Green function
H	= volume specific enthalpy
I	= electric current
$\boldsymbol{j}$	= current density
k	= Boltzmann constant
k_{*j}	= reaction rate
m	= particle mass
$\dot{m}$	= mass flow rate
n	= particle density
$\boldsymbol{n}$	= normal vector
P	= power
p	= pressure
Q	= collision cross section
$\boldsymbol{q}$	= flowfield vector
R_c	= coil radius
R_0	= inner tube radius
r	= radial coordinate
$\boldsymbol{r}$	= spatial vector
T	= temperature
t	= time
u	= z-velocity component
v	= r-velocity component
$\boldsymbol{v}$	= velocity
z	= axial coordinate
α	= heat transfer coefficient
Γ	= inner wall surface
γ	= adiabatic coefficient
ϵ_i	= ionization energy
ε_0	= permittivity of vacuum
η	= viscosity coefficient
κ	= ratio of specific heats
Λ	= inflow boundary surface
λ	= thermal conductivity
μ	= reduced mass
μ_0	= permeability of vacuum
ν	= stochiometric coefficient
ϱ	= mass density
Σ	= outflow boundary surface
σ	= electric conductivity
$\bar{\bar{\tau}}$	= viscous stress tensor
ϕ	= diameter
ψ	= mole fraction
ω	= operation frequency
ω_i	= chemical source term

Subscripts

ch	= chemical
e	= electron
i	= species
ion	= ion
j	= species
m	= tube material
r	= radial
th	= thermal
tot	= total
z	= axial
θ	= azimuthal
ν	= heavy particles

Presented as Paper 98-2947 at the AIAA/ASME 7th Joint Thermophysics and Heat Transfer Conference, Albuquerque, NM, 15–18 June 1998; received 6 July 1999; revision received 15 February 2000; accepted for publication 25 February 2000.

*Ph.D. Candidate, Institut für Raumfahrtsysteme; currently Research Assistant, Institut für Weltraumsensorik und Planetenerkundung, DLR, Rutherfordstr. 2, D-12489 Berlin, Germany; stephan.lenzner@dlr.de.

†Professor, Head of Electric Propulsion and Plasma Technology, Institut für Raumfahrtsysteme, Pfaffenwaldring 31; auweter@irs.uni-stuttgart.de. Senior Member AIAA.

‡Ph.D. Candidate, Institut für Raumfahrtsysteme, Pfaffenwaldring 31; heierman@irs.uni-stuttgart.de. Member AIAA.

§Senior Scientist, Erwin-Schrödinger-Str. 49; sleziona@itwm.uni-kl.de.

Introduction

At the Institute of Space Systems of the University of Stuttgart, an inductively heated plasma wind tunnel is in operation to perform reentry simulations for the development and qualification of heat protection materials for space vehicles.[1] One of the advantages of this facility compared to arc-heated plasma sources is the absence of metal vapor in the plasma, which can arise from cathode erosion in arc-heated plasma sources. With this kind of plasma source, plasmas of highly reactive gases, such as pure oxygen or carbon dioxide, can be produced to simulate the entry into atmospheres of other celestial bodies.

A very important design criterion for this kind of plasma source is to maximize the jet enthalpy at a given electric power input level because high enthalpy plasma flows are desired for reentry simulations. One major difficulty in operating the plasma source at a high-power level arises from the necessity to cool the confinement tube due to heat fluxes to the inner tube wall. The maximum operation temperature of the inner side of the confinement tube sets further limits on the operational power level of the plasma source.

For the design of this plasma source, a numerical code is required that computes the electrodynamic, thermal, chemical and flow quantities of the plasma flow in the discharge region of the plasma source. With these results, the electric input power, the jet enthalpy (thermal, kinetic, and chemical portions), and the heat flux to the confinement tube can be computed. The electric input power is distributed in jet enthalpy and heat flux to the confinement tube, inasmuch as energy losses due to thermal radiation of the plasma are neglected in this low-pressure regime. From these computed energy partitions, the thermal efficiency can be computed for a given rf plasma source.

The numerical code developed for this purpose is based on a simulation code for the investigation of the plasma flow properties in magneto-plasmadynamic (MPD) thrusters.[2] The code to investigate the plasma flow properties of the rf discharge has been modified by replacing the electrodynamic module of the MPD-thruster discharge by one designed to compute the discharge in a rf plasma source. The major difference between these two devices arises from the entirely different electromagnetic fields that drive the plasma discharges in both devices. The electromagnetic fields of the rf discharge are time-dependent fields, which require a complex vector potential approach as described by Mosthagimi and Boulus.[3] Unlike Mosthagimi and Boulus[3] and others,[4,5] who investigated the rf discharge at atmospheric pressure conditions where the flow is entirely subsonic and can be treated with a set of elliptic differential equations, the flow solver of this code is based on a high-order finite volume upwind scheme that allows computation of sub- and supersonic flows.

Because of the high plasma velocities produced by this plasma wind tunnel, Ohm's law for plasmas including the $\boldsymbol{v} \times \boldsymbol{B}$ term has to be implemented in the equations describing the electrodynamic properties of the rf discharge. Unlike under atmospheric pressure conditions where the assumtion of local thermal equilibrium holds, this code distinguishes between electron and heavy particle temperatures because they differ widely under the low-pressure conditions in this plasma source.[4]

A code that is based on the framework of Kelliget and El-Kaddah,[5] Boulos,[6] Mekideche,[7] and Mosthagimi and Boulus[3] and that computes plasma state properties under atmospheric pressure conditions under the assumption of local thermal equilibrium is equipped with a module that computes the stationary heat conduction equation inside the material of the confinement tube to predict the heat flux to the confinement tube and the temperature profile of the inner tube wall. This code was used to perform parameter studies, and there are also plans to use the code in the low-pressure regime. This requires further efforts to increase the computation speed of the low-pressure code.

This paper presents local distributions of electromagnetic, thermal, and flow properties under low-pressure conditions for reentry simulations. The parameter studies presented here are performed with an atmospheric pressure code. These are a power over coil-current plot and a thermal efficiency plot with respect to the operation frequency.

Computational Model

The proposed model is an extension of the work of Mosthagimi and Boulus,[3] Mosthagimi et al.,[4] and Sleziona et al.[2] In this section, the governing equations of the plasma flow inside the rf plasma source, as well as the vector-potential formulation of the discharge equation, the electron-energy equation, and the flowfield equation, are discussed. The flow is assumed to be laminar, and energy losses due to thermal radiation of the plasma are neglected due to the low-pressure regime. The plasma is assumed to be quasi neutral, and the governing equations are implemented in the code in two dimensions due to the rotational symmetry of the configuration.

Flowfield

For the description of the axisymmetric, viscous flow, the following form of the Navier–Stokes equations has been used. These equations were calculated for the three-dimensional grid, which resulted from a rotation of the two-dimensional grid in the azimuthal direction of the cylindrical coordinates.

The total mass conservation equation

$$\frac{\partial}{\partial t}\rho + \nabla \cdot \rho \boldsymbol{v} = 0 \tag{1}$$

is solved for a verification of the species conservation equations.

The total momentum conservation equation is

$$\frac{\partial}{\partial t}\rho \boldsymbol{v} + \nabla \cdot \rho \boldsymbol{v} \otimes \boldsymbol{v} = \nabla \cdot (-p\bar{\bar{I}} + \bar{\bar{\tau}}) + \overline{\boldsymbol{j} \times \boldsymbol{B}} \tag{2}$$

for a plasma flow, which is influenced by electromagnetic fields due to the phasor-averaged $\overline{\boldsymbol{j} \times \boldsymbol{B}}$ forces. The components of the viscous stress tensor are computed with a Newtonian fluid assumption and a pressure and temperature dependent viscosity coefficient:

$$\tau_{\theta\theta} = \eta\left(2\frac{v_r}{r} - \frac{2}{3}\nabla \cdot \boldsymbol{v}\right), \qquad \tau_{rr} = \eta\left(2\frac{\partial v_r}{\partial r} - \frac{2}{3}\nabla \cdot \boldsymbol{v}\right)$$

$$\tau_{rz} = \eta\left(\frac{\partial v_z}{\partial r} + \frac{\partial v_r}{\partial z}\right), \qquad \tau_{zz} = \eta\left(2\frac{\partial v_z}{\partial z} - \frac{2}{3}\nabla \cdot \boldsymbol{v}\right) \tag{3}$$

The total energy conservation equation for the heavy particles of the plasma flow is

$$\frac{\partial}{\partial t}e_{\text{tot}} + \nabla \cdot (H\boldsymbol{v}) = \nabla \cdot (\bar{\bar{\tau}}\boldsymbol{v}) + \nabla \cdot \lambda \nabla T$$

$$+ \nabla \sum_{s=1}^{n} H_s D_s \nabla \psi_s + \sum_{v=1}^{n} n_v n_e \alpha_{ev}(T_e - T_v) \tag{4}$$

The viscous fluxes were extended to obtain the heat fluxes in the translational degrees of freedom. An enthalpy transport due to the mass diffusion is also included. The heating of the heavy particles by the electrons is contained in the compensation between both components by the last term in this equation. The total pressure is obtained by using

$$p = (\gamma - 1)\left[e_{\text{tot}} - \tfrac{1}{2}\rho(u^2 + v^2)\right] + n_e k T_e \tag{5}$$

Herein the adiabatic coefficient γ is a constant ratio of specific heats.

By inspection of the Navier–Stokes equations, it is obvious that the ratio of specific heats occurs only in the energy equation

$$\frac{\partial e_\kappa}{\partial t} + \nabla \cdot [(e_\kappa + p)\boldsymbol{v}] = \nabla \cdot (\bar{\bar{\tau}}\boldsymbol{v}) + \nabla \cdot \lambda \nabla T \tag{6}$$

The index κ indicates that the specific energy is also a function of κ, being a variable depending on p and ρ:

$$e_\kappa = p/(\kappa - 1) + \rho(q^2/2) \tag{7}$$

Next, another specific energy is defined with a constant ratio of specific heats $\gamma = \text{const}$:

$$e_\gamma = p/(\gamma - 1) + \rho(q^2/2) \tag{8}$$

The difference of both specific energies is then

$$Q = e_\kappa - e_\gamma = p\{[1/(\kappa - 1)] - [1/(\gamma - 1)]\} \tag{9}$$

By the replacement of e_κ with $e_\kappa = e_s + Q$, the calculated energy equation then reads

$$\frac{\partial e_\gamma}{\partial t} + \frac{\partial Q}{\partial t} + \nabla \cdot [(e_\kappa + p)\boldsymbol{v}] + \nabla \cdot (Q\boldsymbol{v}) = \nabla \cdot (\bar{\bar{\tau}}\,\boldsymbol{v}) + \nabla \cdot \lambda \nabla T \tag{10}$$

Because only the steady state is of interest, the partial time derivation $\partial Q/\partial t$ can be neglected. Because of this implementation of the real gas effects, the Riemann solver for the flowfield does not need to be changed inasmuch as γ is constant.

Chemical Reactions

For the considered case, the medium argon was taken as fluid. The four species e, Ar, Ar^+, and Ar^{2+} are modeled by four chemical reactions. The species conservation equations, here in mass density form,

$$\frac{\partial c_i}{\partial t} + \nabla c_i \cdot \boldsymbol{v} = w_i + \nabla c_i D_s \nabla \psi_s \tag{11}$$

have to be solved to obtain the chemical composition for chemical nonequilibrium. Here c are the molar concentrations, index i are the species, and the source term w is the chemical production rate of the species. Departing from the general form of the chemical reactions, we have

$$\sum_{i=1}^{n} \nu'_{ij} X_i \rightharpoonup \sum_{i=1}^{n} \nu''_{ij} X_i \tag{12}$$

with ν'_{ij}, ν''_{ij} being the stochiometric coefficients of the component i in the reaction j. X_i is the chemical symbol of the component i. The reaction rates ω_i in molar concentration form are now obtained by using

$$\omega_i = \sum_{j=1}^{m} (\nu''_{ij} - \nu'_{ij}) \left(k_{fj}(T_v, T_e) \prod_i c_i^{\nu'_{ij}} - k_{bj}(T_v, T_e) \prod_i c_i^{\nu''_{ij}} \right) \tag{13}$$

with the molar concentration c_i for the component i and $k_{fj}(T_v, T_e)$ and $k_{bj}(T_v, T_e)$ being the forward and backward reaction coefficients, respectively. They are obtained, appropriate to the considered two-temperature cases, by using the model of Lotz.[8,9]

To achieve a time-step size that is significant for the flowfield and because the characteristic time step of the system of ω_i is considerably smaller, the source terms were integrated with subincremented time steps.

The subincremented integration of the system of nonlinear differential equations ω_i is performed by a Kaps–Rentrop scheme, an implicit scheme that proved to be fast and accurate for this numerically stiff system of differential equations.

Electron Energy Equation

The electron temperature has a considerable effect on the chemical reaction rates and a strong effect on the electrical and thermal conductivity and on the electron density, which again influences the discharge pattern. Under low-pressure conditions for a reentry simulation, the electron temperature differs strongly from the temperature of the heavy particles and has to be treated separately.[4] Therefore, a two-dimensional code for the electron temperature distribution, corresponding to the two-dimensional discharge code, was written. The electron temperature distribution is determined by the thermal energy equation for the electron component:

$$\nabla \cdot (\lambda_e \nabla T_e) + \frac{5}{2}\frac{k}{e}\boldsymbol{j} \cdot \nabla T_e + p_e \nabla \boldsymbol{v} = \frac{\overline{j^2}}{\sigma} - \epsilon_{\text{ion}} \left.\frac{\partial n_e}{\partial t}\right|_{rct} - \sum_{\nu=1}^{n} n_\nu n_e \alpha_{e\nu}(T_e - T_\nu) \tag{14}$$

The first term on the left-hand side represents the conductive heat flux in the electron gas, the second term gives the convective heat flux of the electron gas due to the electron drift. The energy input due to ohmic heating is represented by the first term on the right-hand side, which is phasor averaged. The reaction losses are given by the second term, where ϵ_{ion} is given by Unsöld.[10] The sum of losses is calculated by the third term on the right-hand side due to the energy transfer from the electron gas to the heavy particles gas. The heat transfer coefficient $\alpha_{e\nu}$ and the thermal conductivity λ_e depend on the electron temperature,[11,12] where the heat transfer coefficient is

$$\alpha_{e\nu} = \left(8\sqrt{2}\,|\,\sqrt{\pi}\right) Q_{e\nu} \sqrt{\mu_{e\nu} k T_{e\nu}} [k/(m_e + m_\nu)] \tag{15}$$

and the thermal conductivity

$$\lambda_e = \frac{15}{8}\sqrt{\frac{\pi}{2}} \frac{n_e k^2 T_e}{\sum_{\nu(=e)} n_\nu Q_{e\nu} \sqrt{\mu_{e\nu} k T_{e\nu}}} \tag{16}$$

In the sum of this conductivity equation, ν also includes the electron component. If $Q_{e\nu}$ is the cross section between the electrons and ions, the Gvosdover cross section (Ref. 13) is used. For $\nu = e$ the collision cross section Q_{ee} can be set equal to the Gvosdover cross section. For $Q_{e\nu}$ being the cross section between electrons and atoms, the Ramsauer cross section is used (Ref. 14). The electric conductivity is computed by

$$\sigma = \frac{3}{8}\sqrt{\frac{\pi}{2}} \frac{e^2 n_e}{\sum_{(\nu \neq e)} n_\nu Q_{e\nu} \sqrt{m_e k T_e}} \tag{17}$$

Integral Energy Parameters

The electric power dissipated into the plasma P_E can be computed by application of the phasor-averaged Poynting theorem:

$$P_E = \int_V \overline{\boldsymbol{j} \cdot \boldsymbol{E}}\, \mathrm{d}^3 r \tag{18}$$

The volume integral in Eq. (18) is taken over the entire discharge region. The jet power P_J can be computed from the difference of the surface integrals over the inflow boundary surface Λ and the outflow boundary surface Σ:

$$P_J = \int_\Sigma \left(\left(\frac{1}{2}\rho \boldsymbol{v}^2 + e_{th} + e_{ch} + p\bar{\bar{1}} + \bar{\bar{\tau}} \right) \boldsymbol{v} + \lambda_\nu \nabla T_\nu \right) \cdot \mathrm{d}\boldsymbol{A} - \int_\Lambda \left(\left(\frac{1}{2}\rho \boldsymbol{v}^2 + e_{th} + e_{ch} + p\bar{\bar{1}} + \bar{\bar{\tau}} \right) \boldsymbol{v} + \lambda_\nu \nabla T_\nu \right) \cdot \mathrm{d}\boldsymbol{A} \tag{19}$$

The first term in the integrand of Eq. (19) denotes the kinetic energy density, the second the thermal energy density, and the third the chemical energy density of the plasma flow. The heat flux of the heavy particle gas through the inflow and outflow boundary is represented in the last term. The mean specific jet enthalpy is computed by division of P_J with the mass flow per unit time $\dot{m}$. If catalytic reactions at the inner confinement tube wall are neglected, the integral heat flux P_W to the inner confinement tube wall is computed by the surface integral over the inner tube surface Γ:

$$P_W = \int_\Gamma \lambda_\nu \nabla T_\nu \cdot \mathrm{d}\boldsymbol{A} \tag{20}$$

Because the electric input power is assumed to distribute only in the energy partitions jet power and heat flux to the wall (thermal plasma radiation is neglected in this low-pressure regime), it follows that

$$P_E = P_J + P_W \tag{21}$$

Heat Conduction Equation

Inside the confinement tube wall, the stationary heat conduction equation is reduced due to the absence of ohmic heating (the tube material is regarded as electric insulator) to a Laplace equation for the temperature of the material T_m if a constant thermal conductivity λ_m of the tube is assumed:

$$\nabla^2 T_m = 0 \tag{22}$$

The outer tube wall is water cooled, and therefore, the temperature at this surface is set to the ambient temperature of the cooling water. At the inner tube wall, the boundary layer Γ between plasma and tube material, the heat flux balance leads to

$$(\lambda_v \nabla T_v - \lambda_m \nabla T_m) \cdot \boldsymbol{n} \mid_\Gamma = 0 \tag{23}$$

In the balance of Eq. (23), catalytical heat flux components due to recombination processes are neglected.

Vector Potential Formulation

The electromagnetic fields and induced current densities of the rf discharge are described by the Maxwell equations (24) and a simplified Ohm's law for plasma flows in Eq. (25):

$$\nabla \cdot \boldsymbol{E} = 0, \qquad \nabla \cdot \boldsymbol{B} = 0, \qquad \nabla \times \boldsymbol{E} = -\frac{\partial \boldsymbol{B}}{\partial t} \tag{24}$$

$$\nabla \times \boldsymbol{B} = \mu_0 \left(\boldsymbol{j} + \varepsilon_0 \frac{\partial \boldsymbol{E}}{\partial t} \right), \qquad \boldsymbol{j} = \sigma(\boldsymbol{E} + \boldsymbol{v} \times \boldsymbol{B}) \tag{25}$$

The Maxwell equations (24) can be transformed into an inhomogeneous wave equation for the vector potential $\boldsymbol{A}$ and the coulomb potential Φ by applying the Lorentz gauge. Because of debye shielding inside the plasma, the coulomb potential inside the discharge region vanishes, and only the wave equation for the vector potential has to be regarded:

$$\frac{1}{c^2} \frac{\partial^2 \boldsymbol{A}}{\partial t^2} - \nabla^2 \boldsymbol{A} = \mu_0 \boldsymbol{j} \tag{26}$$

Because the vector-potential $\boldsymbol{A}$ is oscillating with the operation frequency ω, the time dependency is expressed as

$$\boldsymbol{A}(\boldsymbol{r}, t) = \boldsymbol{A}(\boldsymbol{r})\, e^{i\omega t} \tag{27}$$

By combining Eqs. (25) and (26) with Eq. (27), the elliptic discharge equation for the complex vector potential $\boldsymbol{A}$ is obtained:

$$\nabla^2 \boldsymbol{A} - i\mu_0 \sigma \omega \boldsymbol{A} + \mu_0 \sigma \boldsymbol{v} \times \nabla \times \boldsymbol{A} + (\omega^2/c^2)\boldsymbol{A} = 0 \tag{28}$$

The last term in Eq. (28) arises from the displacement current in Maxwell's equations. In the regarded low-frequency regime, it is neglectible compared to the other terms in Eq. (28). Once the solution for $\boldsymbol{A}$ is obtained, the electric field strength $\boldsymbol{E}$ and the magnetic flux density $\boldsymbol{B}$ can be computed from $\boldsymbol{A}$ by

$$\boldsymbol{E} = -i\omega \boldsymbol{A}, \qquad \boldsymbol{B} = \nabla \times \boldsymbol{A} \tag{29}$$

Boundary Conditions

For the flowfield and the species conservation, all values at the inflow boundary are determined to satisfy a given temperature distribution and a fixed argon mass flow rate. The outflow boundary is considered as a freestream boundary, and either the independent flow variables are completely extrapolated for the case of supersonic condition or the energy e_{tot} is calculated with the other extrapolated independent variables and a given pressure for the case of subsonic condition. For the symmetry axis, a no flux condition is taken. This is done by an extrapolation of the density and energy, $\nabla \rho \cdot \boldsymbol{n} = 0$, $\nabla c_i \cdot \boldsymbol{n} = 0$, $\nabla e_{\text{tot}} \cdot \boldsymbol{n} = 0$, and $\nabla e_v \cdot \boldsymbol{n} = 0$, a reflection of the tangential velocity, and setting the normal velocity to zero, $\boldsymbol{v} \cdot \boldsymbol{n} = 0$. The identical boundary condition is taken for the mass, species, and momentum conservation equation at all solid body walls. The boundary condition at the walls for the heavy particles energy is determined by a calculated wall temperature. This temperature is calculated by the heat conduction equation Eq. (22) with the boundary condition Eq. (23).

The electron temperature boundary condition is given by $\nabla T_e \cdot \boldsymbol{n} = 0$, where $\boldsymbol{n}$ is the normal vector of the surfaces. Because of the axial symmetry, $(\partial T_e / \partial r) = 0$ on the axis.

The boundary conditions for the complex vector potential $\boldsymbol{A}$ in the discharge equation Eq. (28) at the inner tube wall are given in cylindric coordinates for an induction coil with n turns as[3]

$$A_\theta(R_0, z) = \frac{\mu_0 I_0}{2\pi} \sum_{i=1}^{n} \sqrt{\frac{R_{ci}}{R_0}} G[k_i(R_{ci}, z_{ci}, R_0, z)]$$

$$+ \frac{\mu_0}{2\pi} \int_{r'=0}^{R_0} \int_{z'=0}^{l_0} \sqrt{\frac{r'}{R_0}}\, j(r', z') G[kk(r', z', R_0, z)]\, \mathrm{d}r'\, \mathrm{d}z'$$

$$k_i(R_{ci}, z_{ci}, R_0, z) = \sqrt{\frac{4 R_{ci} R_0}{(R_{ci} + R_0)^2 + (z - z_{ci})^2}}$$

$$kk(r', z', R_0, z) = \sqrt{\frac{4 r' R_0}{(r' + R_0)^2 + (z - z')^2}} \tag{30}$$

The first term in Eq. (30) represents the portion of the azimuthal vector potential at the inner tube wall induced by the current in the induction coil turns, whereas the second term is the portion arising from the induced current density inside the plasma. The integrated Green functions $G[k_i(R_{ci}, z_{ci}, R_0, z)]$, and $G[kk(r', z', R_0, z)]$ are computed by

$$G(k) = \frac{(2 - k^2)K(k) - 2E(k)}{k}$$

$$K(k) = \int_0^{\pi/2} \frac{\mathrm{d}\varphi}{\sqrt{1 - k^2 \sin^2 \varphi}}$$

$$E(k) = \int_0^{\pi/2} \sqrt{1 - k^2 \sin^2 \varphi}\, \mathrm{d}\varphi \tag{31}$$

The expressions $K(k)$ and $E(k)$ are known as the elliptical integrals of first and second kind. At the inflow and outflow boundary, similar expressions hold.

Computational Method

For the calculation of the rf plasma source flow, all differential equations are solved with a modular program system. The modular code segments are connected iteratively in the following manner: For a given flowfield, chemistry and electron temperature distribution, the current, and, hence, the vector potential distribution were determined. The integrated Green functions in Eq. (30), only dependent on the geometry of the discharge region, are essential for the boundary conditions for the vector potential and are computed in a preprocessing routine. With the ohmic heating, as a result of the current distribution, an electron energy calculation follows and determines a new electron temperature distribution. After this, the flowfield equations were calculated. In the next time step, this new flowfield, including the new chemistry, heavy particle temperature, and the new electron temperature distribution, was taken to calculate the new electromagnetic field distribution, and so on.

In the present program system, the elliptical, partial differential equations for the discharge equation (28) and the electron energy equation (14) are solved with a finite difference method. The discretization yields a nonlinear equation that is iteratively solved by a successive overrelaxation algorithm. The nonlinear, hyperbolic, partial differential equations for the flowfield are solved by a finite volume solver.[2] This code was modified for a nonequilibrium state and for the electromagnetic source terms interaction. The finite volume solver uses a Godunov upwinding scheme for the flux

discretization. The relaxation is done by an explicit time-stepping procedure.

All equations used for the iteratively solved high enthalpy flow, which is influenced by an electrodeless discharge and a magnetic field, are coupled completely by corresponding source terms. This correlates the different physical processes and their conservation equations to one another. That the equations are solved by different solution procedures does not reduce the coupling intensity among the equations; it rather represents a solution and modular development strategy. These individual solution procedures enable an easy implementation of different physical processes and a faster and more exact calculation for several processes. However, a faster calculation is possible because either not all processes need extensive calculation procedures or the step size does not need to be reduced to the value of the slowest equation. With an individual procedure, the calculation and the boundary conditions can be adjusted more exactly for various problems.

Solution of an Example Case

The solution presented was calculated for a flow that had been heated up and accelerated by an rf plasma source. This plasma source was operated with a current coil amplitude of 390 A and an operation frequency of 600 kHz. The mass flow rate of argon was 1 g/s, the ambient pressure in the vacuum chamber was 100 Pa. Figure 1 shows the components of this plasma source as energy supply, capacitor unit, induction coil, and plasma confinement tube. Also the sizes of the components are shown in Fig. 1 as the length of 30 cm and the radius of 8 cm of the tube and the length of 12 cm of the 5-turn induction coil. In this case, the electric input power, computed with Eq. (18), is 56 kW.

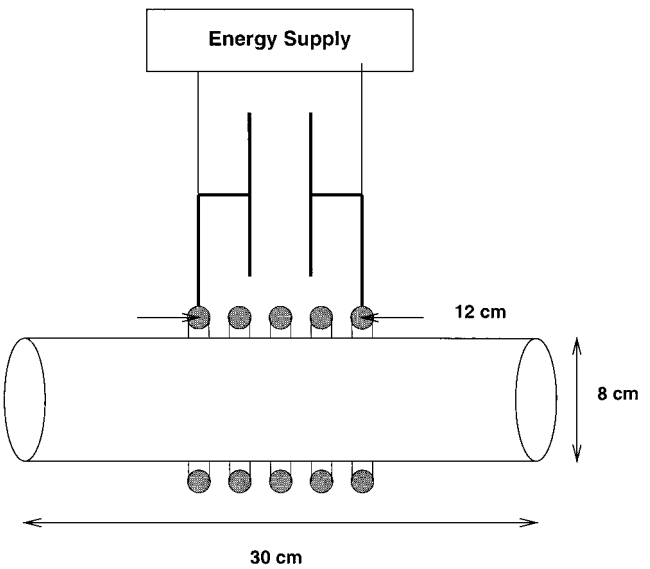

Fig. 1 Radio-frequency plasma source.

Numerical Results

The computation was performed on a structured grid, shown in Fig. 2, with 103 nodes in the axial and 39 nodes in the radial direction. This grid illustrates the computation domain and the contour of the plasma source. The grid is exponentially densed in the radial direction to obtain a sufficient resolution toward the plasma source walls because strong gradients in the flow quantities occur there.

In Fig. 3, the computational results of the electron and heavy particle temperatures are shown. The region of the strongest thermal nonequilibrium occurs at the inner tube wall inside the induction coil due to maximum ohmic heating and a moderate wall temperature in this region, which causes a strong gradient in the heavy particle temperature torward the confinement tube wall, while the electron temperature is adiabatic at the wall. This requires fine-grid resolution at the inner tube wall. Also in this region, the maxima of both temperatures occur. Both temperature distributions are shifted out of the coil center due to the plasma flow. The minimum of the electron temperature is located at the inflow boundary on the symmetry axis. The lowest value of the heavy particle temperature (300 K) is located at the inflow boundary of the computation domain.

In Fig. 4 the plasma velocity and the static pressure distribution are shown. The plasma velocity increases significantly at the first coil turn close to the inner tube wall. Farther downstream, the acceleration propagates toward the symmetry axis. In agreement with this acceleration behavior, the pressure remains almost constant in the inflow boundary, the region between the inflow boundary and the first coil turn. The plasma is created and accelerated in the discharge region inside the induction coil. The pressure gradient in radial direction is caused by the phasor-averaged $\overline{\boldsymbol{j} \times \boldsymbol{B}}$ forces (pinch effect), which is shown in Fig. 5.

In Fig. 5, the phasor-averaged electric input power density $\overline{\boldsymbol{j} \cdot \boldsymbol{E}}$ and the electromagnetic force density $\overline{\boldsymbol{j} \times \boldsymbol{B}}$ are shown. The electric input power density reaches its highest value very close to the confinement tube wall and declines greatly inside the discharge region. This gives rise to the positions of the maxima of the electron temperature and the heavy particle temperature, also close to the confinement tube wall, as shown in Fig. 3. The vectors of the electrodynamic force density acting on the plasma flow are mostly directed radially inward and cause the pinch effect in the pressure distribution, as shown in Fig. 4. Also in this case, the maximum value of this quantity is reached in the region next to the confinement tube inside the induction coil.

The distributions of the electric conductivity and the degree of ionization are shown in Fig. 6. The maxima of both quantities are located where the electron temperature also reaches a maximal value. The maximum value of the degree of ionization of 90% indicates an almost fully ionized plasma state at this location.

The magnitude of the electric field strength in the case of a perfect vacuum inside the tube ($\sigma = 0$) and for the computed plasma state is shown in Fig. 7. Because of the effect of electromagnetic shielding of the plasma, the decline of the electric field is greater toward the symmetry axis in the case of a plasma inside the tube than in the case of a perfect vacuum inside the tube. In the case of a plasma, the axial symmetry of the electric field distribution is perturbed because in

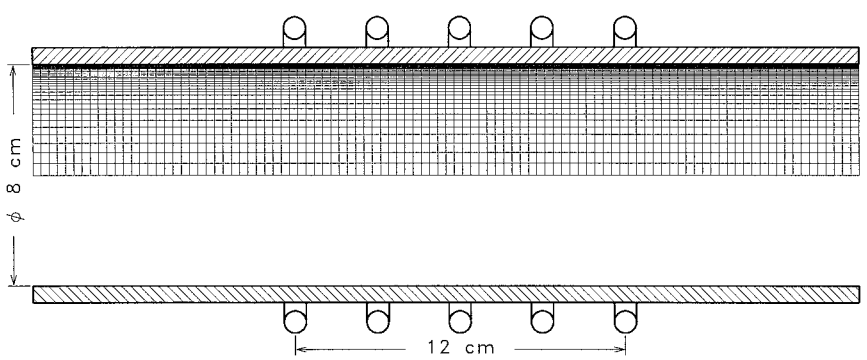

Fig. 2 Computational grid.

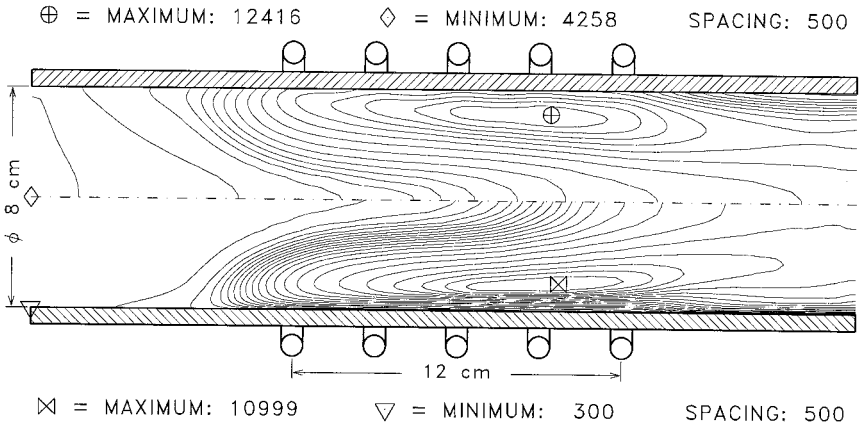

Fig. 3 Electron temperature (Kelvin) (top) and heavy particle temperature (Kelvin) (bottom).

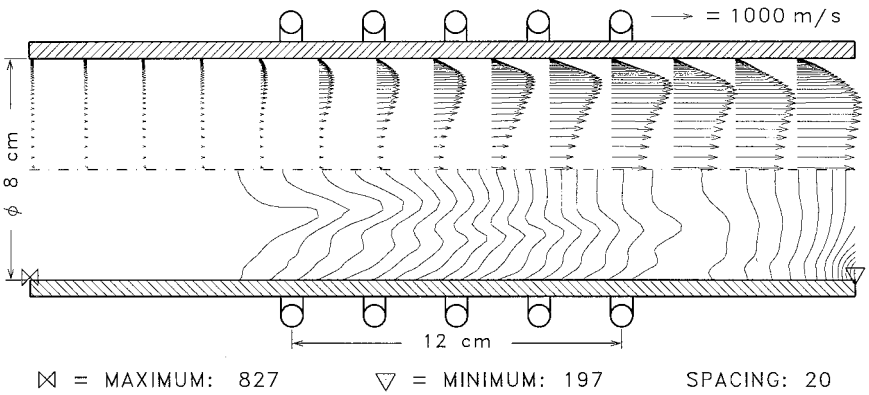

Fig. 4 Velocity vectors (meters per second) (top) and static pressure (pascal) (bottom).

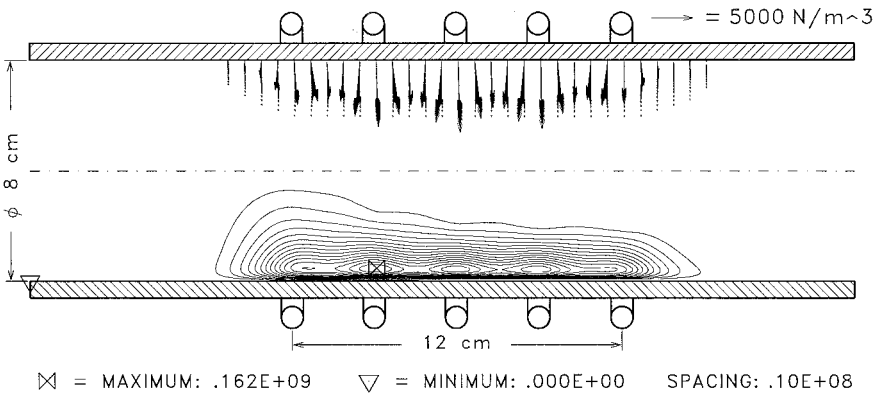

Fig. 5 Electrodynamic force density (newtons per cubic meter) (top) and electric power density (joules per second per cubic meter) (bottom).

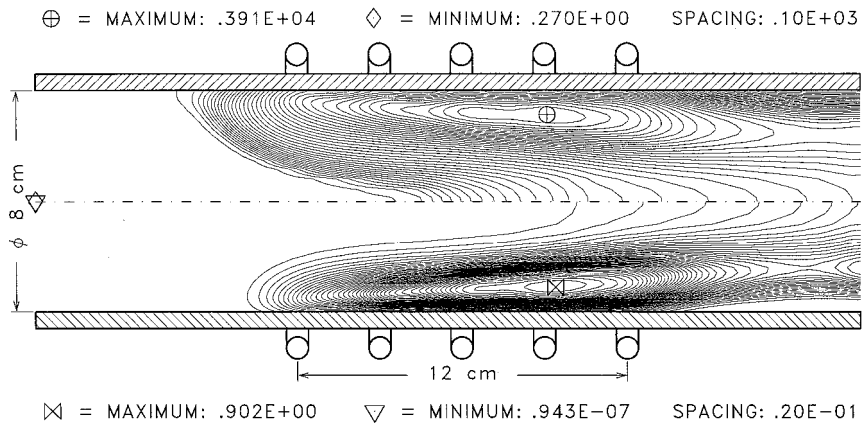

Fig. 6 Electric conductivity (siemens per meter) (top) and degrees of ionization (bottom).

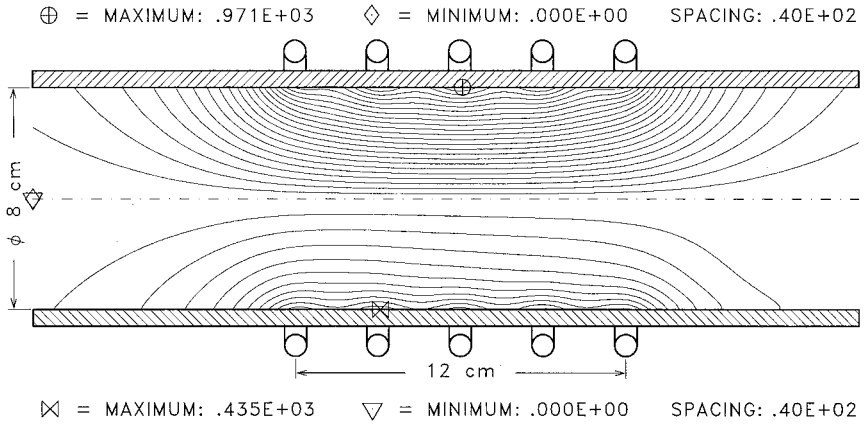

Fig. 7 Electric field strength in perfect vacuum (volts per meter) (top) and in plasma (volts per meter) (bottom).

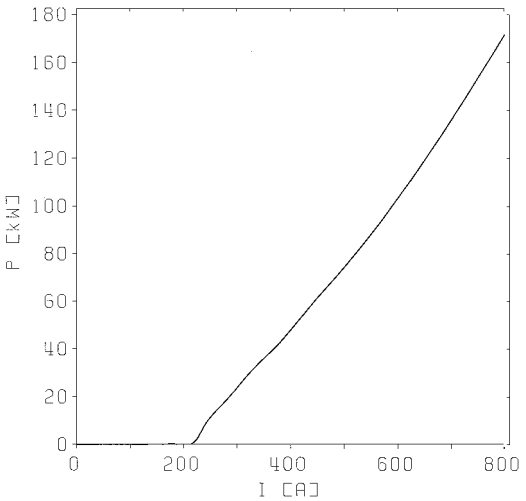

Fig. 8 Electric input power (kilowatts) over current coil amplitude (amperes).

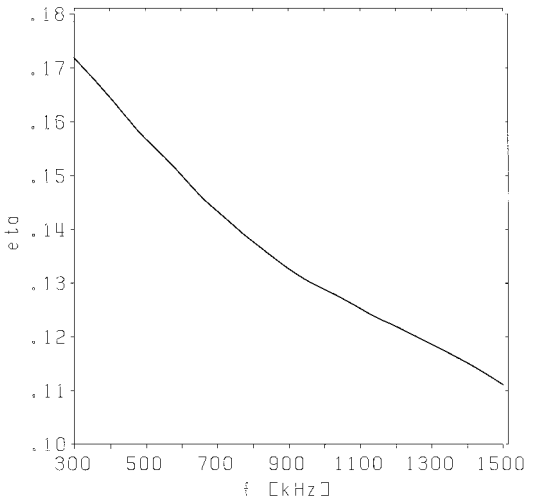

Fig. 9 Thermal efficiency over operation frequency [1/*s*].

the exit region of the coil the electron temperature is larger than in the entrance region of the coil. Therefore, the electric conductivity behaves similarly as shown in Fig. 6 and the electric field in the exit region is more strongly absorbed.

Under atmospheric pressure conditions two parameter studies have been performed for an argon discharge with a mass flow rate of 1 g/s. One is the computation of the electric input power with respect to the coil current amplitude at an operation frequency of 600 kHz. If the current coil amplitude is lowered below 220 A, the discharge extinguishes due to the shifting of the temperature distribution out of the coil by the flow and thermal conduction effects. Below a plasma temperature of 6000 K, the electric conductivity of an argon plasma at atmospheric pressure almost vanishes[15] and no electric energy can be dissipated into the plasma anymore. The discharge can only be sustained if the temperature can be kept above 6000 K in a portion of the discharge region that is sufficiently large. The result is shown in Fig. 8.

The other parameter study performed under atmospheric pressure conditions is the computation of the thermal efficiency of the plasma source, defined as P_J / P_E as given in Eqs. (19) and (18), with respect to the operation frequency $\omega/2\pi$. The electric input power was kept constant at a level of 80 kW. As the operation frequency is lowered, the thermal efficiency rises due to the larger penetration depth of the electromagnetic fields, which causes a better heating of the plasma inside the discharge region and decreases the heat flux to the confinement tube wall. Because of strong energy losses to the confinement tube wall and thermal radiation losses (under atmospheric pressure conditions no longer neglectible), the maximum value is less than 20% at the lowest value of the frequency interval at 300 kHz. The result is shown in Fig. 9.

The flow is assumed to be laminar throughout the discharge region as the Reynolds number drops to a value less than 100 due to the viscosity of the plasma. Also no recirculation inside the flow was observed, unlike computations by Abeele and Degrez.[16] The main difference between the plasma source modeled by Abeele and Degrez and the Institut für Raumfahrtsysteme plasma source is the way the cold gas is injected inside the tube. In the device described in Ref. 16, the gas is injected through a slot between the inner radius of the discharge tube and a shielding plate. This obviously creates recirculations that are carried downstream in the flow and increases their magnitude of velocity as the gas is heated up inside the induction coil. The injection in our device is designed so that the inflow is almost homogeneous, and the creation of recirculations does not occur.

Conclusions

The codes described in this paper were developed and tested to gain a more profound understanding of the fundamental processes occurring in an rf plasma source, especially under low-pressure conditions.

Further development to increase the computational speed has to be done to perform parameter studies as has already been done under atmospheric pressure conditions. One goal of these parameter studies is to maximize the thermal efficiency of this plasma source for the purpose of design criteria. Important integral parameters of this plasma source are the partitions of the electric input power as heat flux losses to the confinement tube wall and total jet enthalpy. A rough comparison of the electrical and thermal properties seems to be possible for the low-pressure case and the atmospheric pressure case because the electric conductivity is only weakly pressure dependent and the temperature distributions in both cases are similar. The parameter studies performed under atmospheric pressure

conditions could give a rough indication about what is to be expected in the desired ones of the low-pressure case.

Acknowledgments

This work was supported by the German Priority Program (Schwerpunktprogramm) "Analysis und Numerik von Erhaltungsgleichungen" of the Deutsche Forschungsgemeinschaft DFG through project "Conservation Equations and Numerical Solutions for Technically Relevant Magneto–Plasmas"(Au 85/9-1,2). The authors thank H. J. Kaeppeler for many discussions and his helpful contributions.

References

[1]Auweter-Kurtz, M., Kurtz, H. L., Laure, S., "Plasma Generators for Re-Entry Simulation," *Journal of Propulsion and Power*," Vol. 12, No. 6, 1996, pp. 1053–1061.

[2]Sleziona, P. C., Auweter-Kurtz, M., and Schrade, H. O., "Computation of MPD Flows and Comparison with Experimental Results," *International Journal of Numerical Methods in Engineering*, Vol. 34, 1992, pp. 759–771.

[3]Mosthagimi, J., and Boulos, M., "Two-Dimensional Electromagnetic Fields in Induction Plasma Modelling," *Plasma Chemistry and Plasma Processing*, Vol. 9, No.1, 1989, pp. 25–44.

[4]Mosthagimi, J., Proulux, P., and Boulos, M., "A Two Temperature Model of the Inductively Coupled RF-Plasma," *Journal of Applied Physics*, Vol. 61, 1987, p. 1753.

[5]Mc Kelliget, J. W., and El-Kaddah, N., "The Effect of Coil Design on Materials Synthesis in an Inductively Coupled Plasma Torch," *Journal of Applied Physics*, Vol. 64, No. 6, 1988, pp. 2948–2954.

[6]Boulos, M.,"The Inductively Coupled Radio Frequency Plasma," *Pure and Applied Chemistry*, Vol. 57, No. 9, 1985, pp. 1321–1352.

[7]Mekideche, M. R., "Contribution a la Modelisation Numerique de Torches a Plasma d'Induction," Ph.D. Dissertation, IUT de Saint-Nazaire, Labortoire de Recherche Techniques Inductives, Université Nantes, Nantes, France, Oct. 1993.

[8]Lotz, W., "An Empirical Formula for the Electron-Impact Ionization Cross-Section," *Zeitschrift für Physik*, Vol. 206, 1967, pp. 205–211.

[9]Lotz, W., "Electron-Impact Ionization Cross-Sections and Ionization Rate Coefficients for Atoms and Ions from Hydrogen to Calcium," *Zeitschrift für Physik*, Vol. 216, 1968, pp. 241–247.

[10]Unsöld, A., *Physik der Sternatmosphären*, Springer-Verlag, Berlin, 1968, pp. 90, 91.

[11]Sleziona, P. C., Auweter-Kurtz, M., Gogel, T., Gölz, T., Messerschmid, E., and Schrade, H., "Non-Equilibrium Flow in Arc Heated Wind Tunnel," edited by J.-A. Desideri, R. Glowinski, and J. Periaux, *Hypersonic Flows for Reentry Problems*, Vol. 2, Springer-Verlag, Berlin, 1991, pp. 1116–1130.

[12]Schrade, H. O., and Sleziona, P. C., "Basic Processes of Plasma Propulsion," Interim Scientific Rept., Air Force Office of Scientific Research, Grant 86-0337, June 1990.

[13]Finkelnburg, W., and Maecker, H., *Elektrische Bögen und thermisches Plasma. Handbuch der Physik, Bd. XXII, Gasentladungen II*, Springer-Verlag, Berlin, 1956, pp. 344–353.

[14]Knoll, M., *Gasentladungstabellen*, Verlag von Julius Springer-Verlag, Berlin, 1935, p. 43.

[15]Devoto, R. S, "Transport Coefficients of Ionized Argon," *The Physics of Fluids*, Vol. 16, No. 5, 1973, pp. 616–623.

[16]Abeele, D., and Degrez, G., "An Efficient Computational Model for Inductive Plasma Flows," AIAA Paper 98-2825, June 1998.